European Journal of Radiology Open 3 (2016) 79–85

Contents lists available at ScienceDirect

European Journal of Radiology Open

journal homepage: www.elsevier.com/locate/ejro

Diffusion-weighted MR imaging of pancreatic cancer: A comparison of mono-exponential, bi-exponential and non-Gaussian kurtosis models

Nikolaos Kartalis[a,b], Georgios C. Manikis[c], Louiza Loizou[a,b], Nils Albiin[a,d], Frank G. Zöllner[e], Marco Del Chiaro[f], Kostas Marias[c], Nikolaos Papanikolaou[a,c,g,*]

[a] Division of Medical Imaging and Technology, Department of Clinical Science, Intervention and Technology (CLINTEC), Karolinska Institutet, Stockholm, Sweden
[b] Department of Radiology, Karolinska University Hospital, Stockholm, Sweden
[c] Laboratory of Computational Medicine, Institute of Computer Science, FORTH, Heraklion, Greece
[d] Department of Radiology, Ersta Hospital, Stockholm, Sweden
[e] Computer Assisted Clinical Medicine, Medical Faculty Mannheim, Heidelberg University, Mannheim, Germany
[f] Division of Surgery, Department of Clinical Science, Intervention and Technology (CLINTEC), Karolinska Institutet and Centre for Digestive Diseases, Karolinska University Hospital, Stockholm, Sweden
[g] Centre for the Unknown, Champalimaud Foundation, Lisbon, Portugal

ARTICLE INFO

Article history:
Received 6 April 2016
Accepted 18 April 2016
Available online 27 April 2016

Keywords:
Pancreas
Pancreatic ductal carcinoma
MRI
Diffusion-weighted MRI

ABSTRACT

Objectives: To compare two Gaussian diffusion-weighted MRI (DWI) models including mono-exponential and bi-exponential, with the non-Gaussian kurtosis model in patients with pancreatic ductal adenocarcinoma.
Materials and methods: After written informed consent, 15 consecutive patients with pancreatic ductal adenocarcinoma underwent free-breathing DWI (1.5T, b-values: 0, 50, 150, 200, 300, 600 and 1000 s/mm^2). Mean values of DWI-derived metrics ADC, D, D*, f, K and D_K were calculated from multiple regions of interest in all tumours and non-tumorous parenchyma and compared. Area under the curve was determined for all metrics.
Results: Mean ADC and D_K showed significant differences between tumours and non-tumorous parenchyma (both $P < 0.001$). Area under the curve for ADC, D, D*, f, K, and D_K were 0.77, 0.52, 0.53, 0.62, 0.42, and 0.84, respectively.
Conclusion: ADC and D_K could differentiate tumours from non-tumorous parenchyma with the latter showing a higher diagnostic accuracy. Correction for kurtosis effects has the potential to increase the diagnostic accuracy of DWI in patients with pancreatic ductal adenocarcinoma.
© 2016 The Authors. Published by Elsevier Ltd. This is an open access article under the CC BY-NC-ND license (http://creativecommons.org/licenses/by-nc-nd/4.0/).

1. Introduction

Diffusion-weighted MR imaging (DWI), a modality that is based on the thermally driven random motion of water molecules (Brownian motion) within tissues, has been used increasingly for the evaluation of a wide variety of solid lesions in the abdomen [1]. Promising results for improved detection and monitoring of therapeutic effects, in terms of prediction and early response assessment, have been reported, amongst others, for the liver [2–10], pancreas [11–13], kidneys [14] and prostate [15,16].

The typical DWI workflow in the clinical practice comprises: (i) qualitative assessment, by visually depicting restricted diffusion in the area of interest compared to the surroundings at different b-values in conjunction with the corresponding apparent diffusion coefficient (ADC) maps, and (ii) quantitative assessment, by measuring various DWI derived biomarkers like ADC, in the organ or area of interest [17]. For the quantitative approach, the two most commonly used models are the mono-exponential-based calculation of ADC and, recently more frequently, the bi-exponential-based estimation of the intravoxel incoherent motion (IVIM)-derived metrics, such as true diffusion coefficient (D), pseudo-diffusion coefficient (D*) and perfusion fraction (f) [18]. The mono-exponential model (monoExp) is more simple to implement, requiring the acquisition of a few b-values and a straightforward linear regression algorithm to fit the data [19]. It is faster to calculate and is provided automatically by the MRI

* Corresponding author. Current address: Centre for the Unknown, Champalimaud Foundation, Avenida Brasília, 1400-038 Lisbon, Portugal.
E-mail addresses: npapan@npapan.com, nikolaos.papanikolaou@fundacaochampalimaud.pt (N. Papanikolaou).

http://dx.doi.org/10.1016/j.ejro.2016.04.002
2352-0477/© 2016 The Authors. Published by Elsevier Ltd. This is an open access article under the CC BY-NC-ND license (http://creativecommons.org/licenses/by-nc-nd/4.0/).

vendors while the bi-exponential model (biExp) is technically more sophisticated requiring multiple b-values (especially in the low b-value range, i.e. 0–200 s/mm^2) and the use of additional software for analysis of data. However, it allows for differentiation of pseudo-diffusion effects and true diffusion effects that are both contributing in the ADC values. Although there is no general consensus regarding the number of b values that needed for IVIM analysis, the suggested minimum number is at least 4, thus making such acquisitions more time-consuming, compared to the 2–3 b-values that are needed for mono-exponential ADC quantification [18].

Although both models, are based on the assumption that the probability displacement function of the water molecules follows a Gaussian distribution, it was observed that in brain DWI applications (reportedly at b-values higher than 1000 s/mm^2), this assumption is not valid [20,21]. Similar findings were recently reported for the liver, kidney, and prostate [22–25]. This is hypothesised to be the result of the interaction of water molecules with membranes and other microstructural components, which in turn reduces the actual diffusion distance compared to free water. The non-Gaussian kurtosis (NGK) model has been shown to take into account tissue heterogeneity and two relative imaging biomarkers namely, the kurtosis coefficient (K) and the corrected diffusion coefficient D_K can be quantified. This approach is technically demanding, time-consuming and requires the acquisition of high and very high b-values [21].

To the best of our knowledge, no studies exist on the application of the non-Gaussian kurtosis model in patients with pancreatic cancer. Therefore, the aim of this prospectively designed study was to compare the three different DWI models, namely the two Gaussian, i.e. mono-exponential (monoExp) and bi-exponential (biExp), and the non-Gaussian kurtosis (NGK) models, for the differentiation of tumours from non-tumorous parenchyma in patients with pancreatic ductal adenocarcinoma (PDAC).

2. Materials and methods

2.1. Study population

This prospectively designed study was approved by the regional ethics review board and written informed consent was obtained from all patients. Within the framework of a different study published elsewhere [26], 16 consecutive patients fulfilled – between May 2010 and May 2011–the following inclusion criteria: a. high suspicion of PDAC, based on clinical history and imaging findings, b. multidisciplinary tumour board decision for surgical treatment with curative intent, c. no history of previous chemo- or radiation therapy, and d. no contraindication for MRI examination.

All patients were enrolled on a preliminary basis. After the exclusion of one patient, whose tumour was histopathologically proven to be other than PDAC (namely gallbladder carcinoma), the final study population comprised 15 patients [mean age ± standard deviation (SD): 64 ± 7 years; age range: 54–77 years; male/female: 8/7] with histopathological proof of PDAC. The lesions had a mean (±SD) diameter of 3.2 ± 0.6 cm and, of them, 12 were located in the head, one in the body and two in the tail of the pancreas.

2.2. MRI technique

All examinations were performed at a clinical 1.5T scanner (Magnetom Avanto, Siemens Healthcare, Erlangen, Germany) with a 12-channel body and spine matrix coil combination. All patients underwent free-breathing single-shot spin-echo echo-planar DWI of the pancreas with 8 different b-values (0, 50, 100, 150, 200, 300, 600 and 1000 s/mm^2). The diffusion gradients were applied in 3 orthogonal axes (tetrahedral scheme), parallel imaging

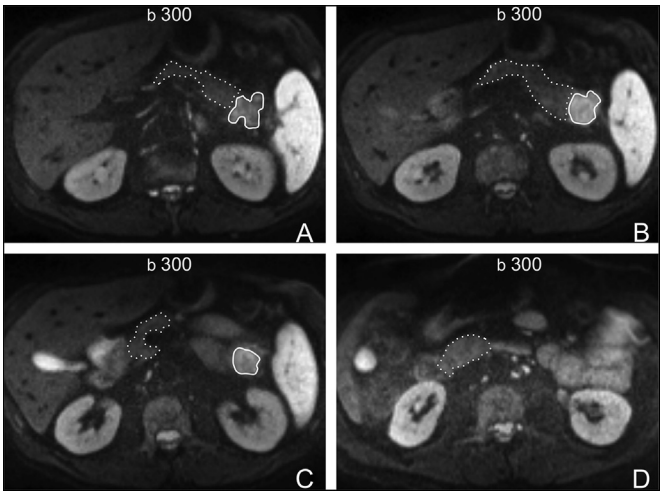

Fig. 1. 65-year-old male patient wth a ductal adenocarcinoma (arrow) at the pancreatic tail. (A– D), Axial DWI images with a b-value of 300 s^2/mm. Multiple regions of interest (ROIs) were carefully drawn on tumour (continuous line) and downstream parenchyma (dashed line) at all levels (A: most cranial level—D: most caudal level). All ROIs were then copied and pasted on all other b-value image series (please see Fig. 2).

factor was 2 and the spectral selective fat saturation pulse was used. The DWI acquisition time was 9 min and 02 s. Details of the MRI protocol parameters are presented in Table 1. In order to maintain sufficient signal-to-noise ratio, 5 averages were chosen for all b-value acquisitions. Coronal, navigator-triggered, T2-weighted HASTE images were obtained before the DWI sequences for optimal slice positioning. No intravenous contrast agent was used. For clinical purposes (preoperative staging and surgical planning), all patients had undergone an additional, dedicated, pancreatic protocol multi-detector CT (MDCT) examination.

2.3. Post-processing and image analysis

The post-processing analysis was performed using the open-source image analysis software OsiriX version 5.6 [27] and the UMMDiffusion plug-in version 0.1 [28,29].

One radiologist (NK) with 6 years' experience in pancreatic imaging carefully drew multiple free-hand regions of interest (ROIs) at all slice levels, in order to encompass as much of the tumour and non-tumorous parenchyma as possible, both upstream and downstream (i.e. to the left and right of the tumour, respectively), avoiding the outmost margins of the lesions/parenchyma in order to minimise partial volume averaging (Fig. 1). There was an effort to avoid the inclusion of vessels and areas of necrosis/cystic changes. The DWI sequence chosen for ROI drawing was the b-value image series where the tumour was best visualised; ROIs were then pasted at all other b-value image series (Fig. 2). For optimal ROI drawing, apart from DWI, all other available images (i.e. T2-weighted HASTE and MDCT) were taken into consideration to account for the relatively low spatial resolution of DWI images and, thus, minimise partial volume effects in the calculations. In that way (i.e. multiple ROIs in both tumour and parenchyma per patient), essentially the whole volume of the tumour as well as both upstream and downstream parenchyma, when possible, was measured in all patients. In total, 85 ROI measurements were performed, of which 36 were tumorous and 49 non-tumorous (21 downstream and 28 upstream). Mean (±SD) ROI size in tumours, upstream, and downstream parenchyma were 4.4 ± 2.5, 8.1 ± 4.1, and 6.4 ± 3.7 cm^2, respectively. Upstream and downstream non-tumorous parenchyma were evaluated separately in order to account for potential differences between these

Table 1
Imaging parameters.

Sequence	Imaging plane	Voxel size (mm)	Slice thickness/gap (mm)	TE (ms)	TR (ms)	Averages
T2-weighted HASTE	Coronal	2.3 × 1.8 × 4	4/0	87	1000	1
T1-weighted in/opposed phase	Axial	2.0 × 1.4 × 4	4/0	5.05/2.37	126	1
DWI	Axial	2.1 × 2.1 × 5	5/0	75	2400	5

Abbreviations: TE = excitation time, TR = repetition time.

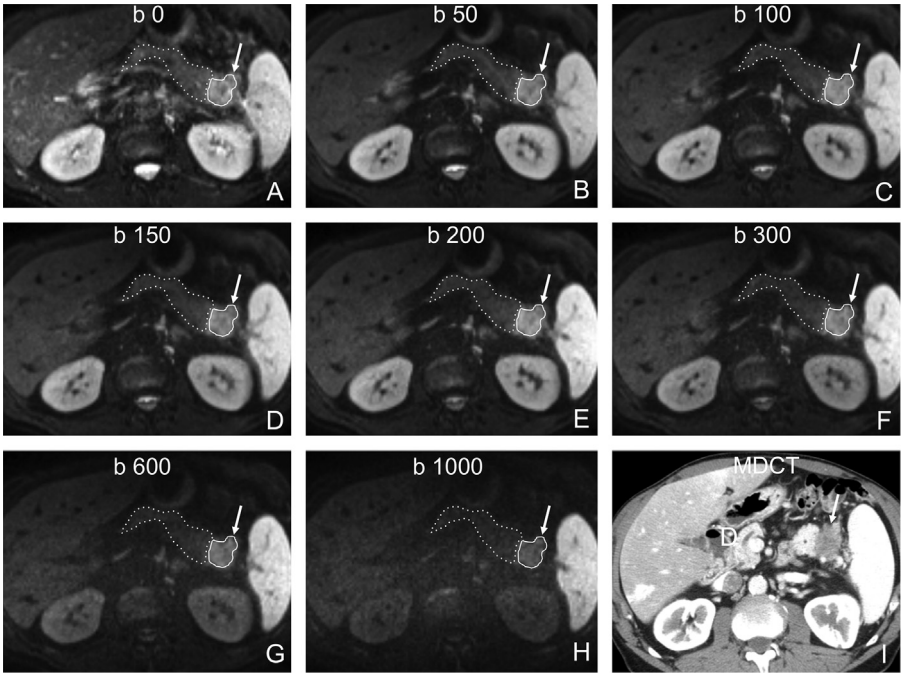

Fig. 2. 65-year-old male patient wth a ductal adenocarcinoma at the pancreatic tail (same patient as in Fig. 1). A–H, Axial DWI images with b-values from 0 A to 1000 s/mm^2 H show restricted diffusion of the tumour (arrow) compared to the adjacent parenchyma. Due to the high number of averages obtained (5), the signal-to-noise ratio in the high b-value images was acceptable (SNR_{tumour} = 8; $SNR_{parenchyma}$ = 4). I, Axial multidector CT (MDCT) image shows the tumour as a relatively well-demarcated hypovascular area. For optimal ROI positioning in tumour (continuous line) and in non-tumorous parenchyma (dashed line), both MDCT I and T2-weighted HASTE images (not shown) were used in conjuction with DWI images A–H in order to compensate for the inherent low resolution of DWI images.

two areas secondary to the presence of changes of obstructive pancreatitis, which is often encountered in the upstream parenchyma and which may alter the microscopic structure, and thus the diffusivity of the tissues [30].

The DWI metrics that were quantified and the corresponding formulae used for the calculation were:

(i) ADC from the monoexponential fit, according to:

$$S(b) = S_0 \exp(-bADC)$$

(ii) D, D* and f from the biexponential fit, according to:

$$S(b) = S_0[(1-f)\exp(-bD) + f\exp(-bD*)]$$

See Ref. [31].

(iii) K and D_K from the non-Gaussian kurtosis fit, according to:

$$S(b) = S_0 \exp(-bD_K + b^2 D_K^2 K/6)$$

See Ref. [21],whereas S(b) is the signal intensity (SI) at a given b-value, S_0 the SI without any diffusion weighting gradient (b-value = 0), ADC the apparent diffusion coefficient, D the true diffusion coefficient, D* the pseudo-diffusion coefficient, f the micro-perfusion fraction, D_K is the diffusion coefficient corrected for kurtosis, and K the kurtosis coefficient. The kurtosis coefficient expresses the grade of deviation from the Gaussian distribution and is a unitless parameter, whose value may be either 0 (expressing perfect Gaussian distribution) or higher. Kurtosis effects were classified as minimal (K < 0.5), intermediate (0.5 < K < 1) or substantial (K > 1). Apart from the ADC maps provided automatically by the scanner's console, no other maps were created and no map analysis was performed.

All the aforementioned models were implemented in the UMMDiffusion plugin. No noise thresholding or similar was performed during the calculation of the parameters and neither was motion correction applied for post-processing purposes. The plugin calculates the mean value within the ROI at each b-value and fits the signal intensity curve to the respective model. For nonlinear least square fitting, the Levenberg-Marquardt algorithm was implemented in the plugin [32,33].

In order to evaluate if the SNR at the images with a b-value of 1000 s/mm^2 was sufficient, SNR_{b1000} was calculated by using the formulae:

$$SNR_{tumour} = SI_{tumour}/\text{noise and } SNR_{parenchyma} = SI_{parenchyma}/\text{noise},$$

whereas SI_{tumour} is the SI of the tumour, $SI_{parenchyma}$ is the SI of the parenchyma and noise is the standard deviation of the SI of the background air measured outside the body.

2.4. Statistical analysis

Descriptive statistics were used to describe the data. Multiple comparisons of continuous data were performed by analysis of variance (ANOVA) and, if there was a statistically significant result, the comparisons were made using the post-hoc Bonferroni

Table 2
DWI metrics of the Gaussian mono-exponential and bi-exponential models as well as the non-Gaussian kurtosis model in tumours and non-tumorous (down- and upstream) parenchyma and their analysis of variance (ANOVA).

DWI metrics	Regions	Number of ROIs	Mean value	Standard deviation	P-value (ANOVA)
ADC (10^{-3} mm^2/s)	Tumour	36	1.435	0.15	<0.0001
	Downstream	21	1.586	0.21	
	Upstream	28	1.663	0.24	
D (10^{-3} mm^2/s)	Tumour	36	0.955	0.31	0.35
	Downstream	21	0.909	0.32	
	Upstream	28	1.045	0.39	
D* (10^{-3} mm^2/s)	Tumour	36	17.76	17.66	0.63
	Downstream	21	22.35	21.38	
	Upstream	28	17.63	19.29	
f	Tumour	36	0.30	0.15	0.32
	Downstream	21	0.35	0.12	
	Upstream	28	0.35	0.16	
K	Tumour	36	1.070	0.16	0.15
	Downstream	21	1.091	0.19	
	Upstream	28	1.003	0.17	
D_K (10^{-3} mm^2/s)	Tumour	36	2.161	0.48	<0.001
	Downstream	21	2.685	0.49	
	Upstream	28	2.752	0.72	

Abbreviations: ADC = apparent diffusion coefficient, D = true diffusion coefficient, D* = pseudo-diffusion coefficient, f = perfusion fraction, K = kurtosis coefficient, D_K = corrected diffusion coefficient.

Table 3
Comparison of the DWI metrics ADC and D_K, which showed statistical significance in the analysis of variance (Table 2), between tumours and downstream and upstream non-tumorous parenchyma.

DWI metrics	Comparison of regions	Mean difference	Standard error	P-value (Bonferroni)
ADC (10^{-3} mm^2/s)	Upstream parenchyma vs. tumour	0.23	0.05	<0.0001
	Downstream parenchyma vs. tumour	0.15	0.05	0.007
	Upstream vs. downstream parenchyma	0.08	0.06	0.72
D_K (10^{-3} mm^2/s)	Upstream parenchyma vs. tumour	0.59	0.15	<0.001
	Downstream parenchyma vs. tumour	0.52	0.13	<0.001
	Upstream vs. downstream parenchyma	0.07	0.18	1

Abbreviations: ADC = apparent diffusion coefficient, D_K = corrected diffusion coefficient.

or Tukey's studentized Range (HSD) analysis. Receiver operator curve (ROC) analysis was performed to determine the area under the curve (AUC) and optimal thresholds for the various DWI metrics for the differentiation of tumours from non-tumorous parenchyma. Goodness-of-fit for each of the three models was assessed using the reduced Chi^2 test. For the calculation of the reduced Chi^2, the mean Chi^2 value was divided by the number of degrees of freedom for each model (number of data points – number of parameters). For monoExp, biExp, and NGK the degrees of freedom were 7, 5, and 6, respectively. All statistical analyses were carried out using the SPSS version 20 package (SPSS Inc., Chicago, IL) and a P-value lower than 0.05 was considered significant.

3. Results

All tumours were visualised on DWI series. In tumours, kurtosis was substantial in 26/36 (72%) and intermediate in 10/36 (28%) of measurements. In non-tumorous parenchyma, substantial kurtosis was present in 27/49 (55%) and intermediate in 22/49 (45%) of measurements. Mean ADC and mean D_K were the only DWI metrics allowing for the differentiation of tumours from non-tumorous parenchyma (Tables 2 and 3). Results of the ROC curve analysis are presented in Tables 4 and Fig. 3 . D_K showed highest diagnostic accuracy with an area under ROC curve of 0.84. For a D_K threshold value of 2.37×10^{-3} mm^2/s, the sensitivity and specificity were 81% and 86%, respectively. Mean (±SD) of reduced Chi^2 for the monoExp, biExp, and NGK were 0.020 ± 0.011, 0.004 ± 0.01, and 0.008 ± 0.008, respectively, for tumorous ROIs ($P < 0.05$, for all pairwise comparisons). For non-tumorous ROIs, mean (±SD) of reduced Chi^2 for the monoExp, biExp, and NGK were 0.059 ± 0.035, 0.004 ± 0.007, and 0.02 ± 0.013, respectively ($P < 0.05$, for all pairwise comparisons). In all patients, plotting the log SI of the original data vs. all b-values used turned triexponential curves. The segment with the steepest SI decay corresponded to the low b-value range, whereas the segment with the least steep SI decay of the three corresponded to the high b-value range. Diagrams of the fitting of the curves of the three models in a patient with a tumour in the pancreatic tail are

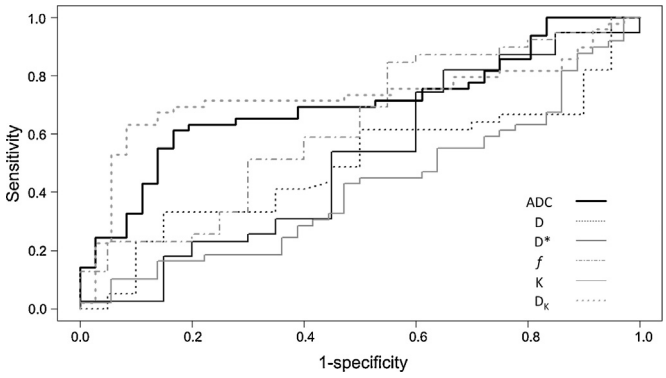

Fig. 3. Diagram representing the receiver operator curve analysis for the DWI metrics' apparent diffusion coefficient (ADC), true diffusion coefficient (D), pseudo-diffusion coefficient (D*), perfusion fraction (f), kurtosis coefficient (K) and corrected diffusion coefficient (D_K) for the differentiation of tumours from non-tumorous parenchyma. The D_K had the larger area under the curve and, together with ADC, reached statistical significance.

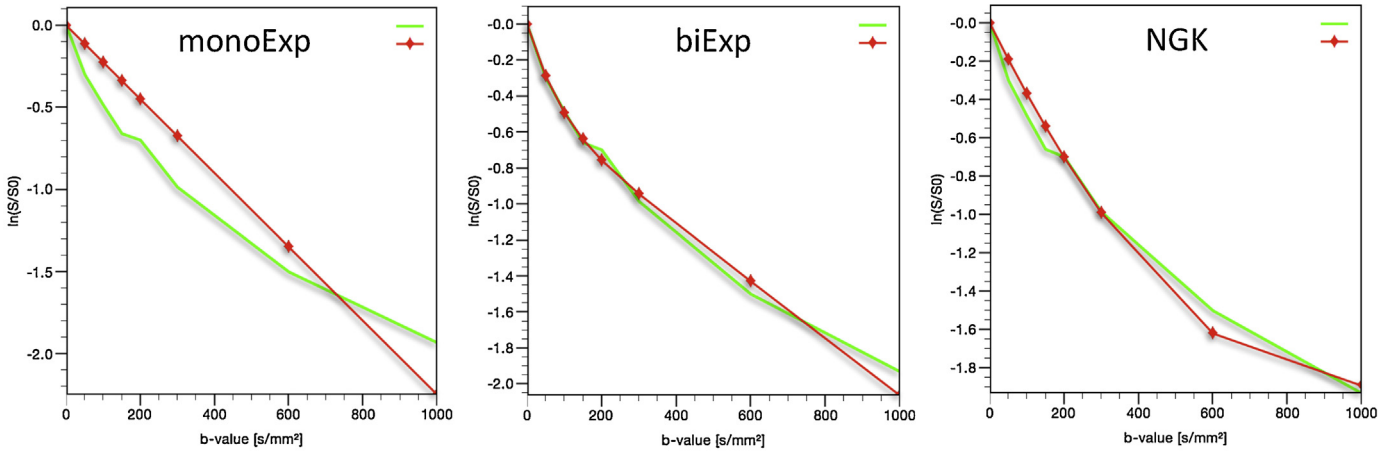

Fig. 4. Diagrams representing the fitting of the curves derived from the three models, i.e. the two Gaussian [mono-exponential (monoExp) and bi-exponential (biExp)] and the non-Gaussian kurtosis (NGK), from a tumour located in the pancreatic tail (same patient as in Figs. 1 and 2). The green line corresponds to the measured signal (original data, identical in all three diagrams) and the red line to the corresponding fitting model. The markers on the red line are for visualisation purposes, in case the curves are too close to each other, and do not represent the measured signal. The UMMDiffusion plugin calculates the mean value within the ROI at each b-value and fits the signal intensity curve to the respective model. (For interpretation of the references to colour in this figure legend, the reader is referred to the web version of this article.).

Table 4
Calculation of area under the curve (AUC) for the DWI metrics ADC, D, D*, f, K, and D_K for the differentiation of tumours from non-tumorous parenchyma.

DWI metrics	AUC	Standard error	P-value
ADC	0.77	0.05	<0.0001
D	0.52	0.06	0.804
D*	0.53	0.06	0.698
f	0.62	0.06	0.072
K	0.42	0.06	0.218
D_K	0.84	0.05	<0.0001

Abbreviations: ADC = apparent diffusion coefficient, D = true diffusion coefficient, D* = pseudo-diffusion coefficient, f = perfusion fraction, K = kurtosis coefficient, D_K = corrected diffusion coefficient.

shown in Fig. 4. Mean values (median, SD, and range) of SNR of the tumours were 9 (9, 2, and 6–14) while of the non-tumorous parenchyma were 6 (6, 2, and 4–11).

4. Discussion

The results of our study, as presented in Tables 2 and 3, showed that for the differentiation of tumours from non-tumorous parenchyma in patients with PDAC, the only DWI metrics showing statistical significance were mean ADC and D_K. Both metrics were significantly lower in tumours compared to non-tumorous tissue. D_K which represents the diffusion coefficient that takes into account kurtosis effects was the DWI metric with the highest diagnostic accuracy for differentiation of tumours versus non-tumorous parenchyma with an area under the ROC curve of 0.84. In agreement with other published reports on both healthy individuals and oncological patients, the mean value of D_K was higher compared to the mono-exponentially-based calculations of ADC [34,35].

The mean values of the IVIM-derived biexponential metrics D and f were higher in the non-tumorous parenchyma than the tumours. However, the differences were not statistically significant. These findings are contradictory to previously reported data. Concia et al. showed that D was significantly higher and f significantly lower in tumours compared to non-tumorous areas and, thus, they were able to differentiate between them [12]. Possible explanations for this inconsistency include differences between the two studies in terms of the histopathological characteristics of included tumours, the number and levels of the acquired b-values and software used for the calculation of the various DWI metrics and, finally, methodological variations in the acquisition of the ROI measurements. Considering the latter, multiple ROI measurements were performed in our study essentially encompassing the whole volume of both the tumour and, wherever feasible, the non-tumorous parenchyma, compared to fewer measurements in tumour and healthy parenchyma performed in the study by Concia et al. [12]. Our results probably indicate that in patients with PDAC differentiation of tumorous from non-tumorous pancreatic tissue based on biomarkers that are sensitive to a combination of micro-perfusion and diffusion effects may be more accurate compared to those sensitive to micro-perfusion or diffusion effects separately. Several previous reports have shown that f could differentiate between patients with PDAC from healthy volunteers [36–39]. However, a direct comparison of the results of these reports with our results is not possible, as our study design was different and no healthy volunteers were enrolled.

Furthermore, in all ROI measurements in our study, K had values greater than 0.5, meaning that kurtosis effects were present in both the tumorous and the non-tumorous ROIs. Substantial kurtosis effects (i.e. K > 1) were detected in 72% of tumorous and 55% of non-tumorous ROIs. Interestingly, the mean K value of the downstream non-tumorous parenchyma was higher compared to both the tumours and the upstream non-tumorous parenchyma (Table 2); however, these differences were not statistically significant. This tendency indicates that microstructural heterogeneity depicted as kurtosis effects is observed not only in tumours but also – to a varying degree – in non-tumorous tissues. A possible explanation for the differences between downstream and upstream non-tumorous parenchyma may be the presence of upstream obstructive pancreatitis [30].

Higher diagnostic accuracy of biomarkers sensitive to the combination of micro-perfusion and diffusion effects, as well as, the presence of at least intermediate kurtosis effects in all ROI measurements may prove to be of importance and need to be addressed, if the role of DWI-derived potential biomarkers is to be explored in further research applications. Such applications include the differentiation of pancreatic adenocarcinoma from mass-forming chronic pancreatitis, the prediction of tumour grade and, finally, the prediction and early assessment of tumour response following neoadjuvant or palliative oncological therapy. Particularly for the differentiation of PDAC from mass-forming chronic pancreatitis, the reported data on the role of mono-exponential-based ADC calculations are contradictory [40,41]. Interestingly, the IVIM-derived perfusion fraction f was shown to be able to differentiate between

the two entities [37]. Contradictory results in the literature exist also regarding the ability of mono-exponential-based ADC calculations to predict adenocarcinoma tumour grade [42,43]. Therefore, for all of the above applications, the use of more sophisticated DWI-derived biomarkers may seem to be useful.

Regarding the comparison of the goodness-of-fit analysis, there were statistically significant differences of the mean values of reduced Chi^2 between the three models. The biExp model provided with the highest fitting performance, followed by NGK and, finally, by monoExp. This is in line with previously reported data [23,24] and supports our hypothesis that kurtosis effects exist in our data although acquired with a maximum b value of only 1000 s/mm^2. In general, very high b-values are recommended for the evaluation of NGK in brain applications [44]. However, in abdominal applications, due to lower SNR and lower T2 relaxation times of the various organs compared to the brain, very high b-values are not usually applied. Recently, various authors have shown that kurtosis effects could be detectable in abdominal and whole-body applications even when using maximum b-values of 800 s/mm^2 or less at 3T [23,24]. We applied multiple b-values with a maximum of 1000 s/mm^2 that, coupled with the use of a parallel imaging factor of 2 and 5 averages, resulted in images with acceptable SNR at 1.5T (Figs. 1 and 2). In tumorous and non-tumorous ROIs, mean SNR at the image series with a b-value of 1000 s/mm^2 were 9 and 6, respectively. The resulting curves of plotting log SI vs. b-values were shown to be triexponential in all patients, where the least steep segment of SI decay of the three corresponded to the high b-value range. The latter might be indicative of the presence of kurtosis effects, even at b-values not exceeding 1000 s/mm^2 that is in agreement with the aforementioned published data [23,24].

Our study has several limitations. Firstly, the study population was relatively small. Despite that, we were able to detect statistically significant differences for the metrics ADC and D_K. Secondly, the effect of inter-reader variation in the ROI positioning was not investigated. However, it has been shown that this variation is not significant in cases of whole-volume measurements, as is the case in our study [45]. Furthermore, motion correction between different b-values was not performed due to software limitations, which may influence the accuracy of the calculations and the cut-off value in the ROC analysis was not defined prospectively, which may falsely increase the accuracy of the results. Finally, the inclusion of patients solely with PDAC precluded the comparison of the three models regarding the differentiation of the various pancreatic pathologies.

In conclusion, the metrics ADC and D_K could differentiate PDAC from non-tumorous parenchyma with the latter showing a better diagnostic accuracy. Correction for kurtosis effects has the potential to increase the diagnostic accuracy of DWI of pancreas in patients with PDAC.

Conflict of interest

All authors disclose no financial support or involvement in organization(s) with financial interest in the subject matter.

References

[1] S. Bonekamp, C.P. Corona-Villalobos, I.R. Kamel, Oncologic applications of diffusion-weighted MRI in the body, J. Magn. Reson. Imaging 35 (2012) 257–279, http://dx.doi.org/10.1002/jmri.22786.
[2] M. Bruegel, K. Holzapfel, J. Gaa, K. Woertler, S. Waldt, B. Kiefer, et al., Characterization of focal liver lesions by ADC measurements using a respiratory triggered diffusion-weighted single-shot echo-planar MR imaging technique, Eur. Radiol. 18 (2008) 477–485, http://dx.doi.org/10.1007/s00330-007-0785-9.
[3] B. Taouli, V. Vilgrain, E. Dumont, J.-L. Daire, B. Fan, Y. Menu, Evaluation of liver diffusion isotropy and characterization of focal hepatic lesions with two single-shot echo-planar MR imaging sequences: prospective study in 66 patients, Radiology 226 (2003) 71–78, http://dx.doi.org/10.1148/radiol.2261011904.
[4] D.M. Koh, E. Scurr, D. Collins, B. Kanber, A. Norman, M.O. Leach, et al., Predicting response of colorectal hepatic metastasis: value of pretreatment apparent diffusion coefficients, Am. J. Roentgenol. 188 (2007) 1001–1008, http://dx.doi.org/10.2214/AJR.06.0601.
[5] Y. Cui, X.P. Zhang, Y.S. Sun, L. Tang, L. Shen, Apparent diffusion coefficient: potential imaging biomarker for prediction and early detection of response to chemotherapy in hepatic metastases, Radiology 248 (2008) 894–900, http://dx.doi.org/10.1148/radiol.2483071407 (pii: 248/3/894).
[6] L. Mannelli, S. Kim, C.H. Hajdu, J.S. Babb, T.W.I. Clark, B. Taouli, Assessment of tumor necrosis of hepatocellular carcinoma after chemoembolization: diffusion-weighted and contrast-enhanced MRI with histopathologic correlation of the explanted liver, Am. J. Roentgenol. 193 (2009) 1044–1052, http://dx.doi.org/10.2214/AJR.08.1461.
[7] I.R. Kamel, E. Liapi, D.K. Reyes, M. Zahurak, D.a. Bluemke, J.-F.H. Geschwind, Unresectable hepatocellular carcinoma: serial early vascular and cellular changes after transarterial chemoembolization as detected with MR imaging, Radiology 250 (2009) 466–473, http://dx.doi.org/10.1148/radiol.2502081988.
[8] M. Wagner, S. Doblas, J.-L. Daire, V. Paradis, N. Haddad, H. Leitao, et al., Diffusion-weighted MR imaging for the regional characterization of liver tumors, Radiology 264 (2012) 464–472, http://dx.doi.org/10.1148/radiol.12111530.
[9] G. d'Assignies, P. Fina, O. Bruno, M.-P. Vullierme, F. Tubach, V. Paradis, et al., High sensitivity of diffusion-weighted MR imaging for the detection of liver metastases from neuroendocrine tumors: comparison with T2-weighted and dynamic gadolinium-enhanced MR imaging, Radiology 268 (2013) 390–399, http://dx.doi.org/10.1148/radiol.13121628.
[10] S. Doblas, M. Wagner, H.S. Leitao, J.L. Daire, R. Sinkus, V. Vilgrain, B.E. Van Beers, Determination of malignancy and characterization of hepatic tumor type with diffusion-weighted magnetic resonance imaging: comparison of apparent diffusion coefficient and intravoxel incoherent motion-derived measurements, Invest. Radiol. 48 (2013) 722–728, http://dx.doi.org/10.1097/RLI.0b013e3182915912.
[11] T. Ichikawa, S.M. Erturk, U. Motosugi, H. Sou, H. Iino, T. Araki, et al., High-b value diffusion-weighted MRI for detecting pancreatic adenocarcinoma: preliminary results, Am. J. Roentgenol. 188 (2007) 409–414, http://dx.doi.org/10.2214/AJR.05.1918.
[12] M. Concia, A.M. Sprinkart, A.-H. Penner, P. Brossart, J. Gieseke, H.H. Schild, et al., Diffusion-weighted magnetic resonance imaging of the pancreas: diagnostic benefit from an intravoxel incoherent motion model-based 3 b-value analysis, Invest. Radiol. 49 (2014) 93–100, http://dx.doi.org/10.1097/RLI.0b013e3182a71cc3.
[13] N. Kartalis, T.L. Lindholm, P. Aspelin, J. Permert, N. Albiin, Diffusion-weighted magnetic resonance imaging of pancreas tumours, Eur. Radiol. 19 (2009) 1981–1990, http://dx.doi.org/10.1007/s00330-009-1384-8.
[14] H. Chandarana, S.K. Kang, S. Wong, H. Rusinek, J.L. Zhang, S. Arizono, et al., Diffusion-weighted intravoxel incoherent motion imaging of renal tumors with histopathologic correlation, Invest. Radiol. 47 (2012) 688–696, http://dx.doi.org/10.1097/RLI.0b013e31826a0a49.
[15] T. Kobus, P.C. Vos, T. Hambrock, M. De Rooij, C.a. Hulsbergen-Van de Kaa, J.O. Barentsz, et al., Prostate cancer aggressiveness: in vivo assessment of MR spectroscopy and diffusion-weighted imaging at 3T, Radiology 265 (2012) 457–467, http://dx.doi.org/10.1148/radiol.12111744.
[16] D.M. Somford, C.M. Hoeks, C.a. Hulsbergen-van de Kaa, T. Hambrock, J.J. Fütterer, J.A. Witjes, et al., Evaluation of diffusion-weighted MR imaging at inclusion in an active surveillance protocol for low-risk prostate cancer, Invest. Radiol. 48 (2013) 152–157, http://dx.doi.org/10.1097/RLI.0b013e31827b711e.
[17] M.C. Maas, J.J. Fütterer, T.W.J. Scheenen, Quantitative evaluation of computed high B value diffusion-weighted magnetic resonance imaging of the prostate, Invest. Radiol. 48 (2013) 779–786, http://dx.doi.org/10.1097/RLI.0b013e31829705bb.
[18] D.M. Koh, D.J. Collins, Diffusion-weighted MRI in the body: applications and challenges in oncology, Am. J. Roentgenol. 188 (2007) 1622–1635, http://dx.doi.org/10.2214/AJR.06.1403.
[19] D.M. Koh, D.J. Collins, M.R. Orton, Intravoxel incoherent motion in body diffusion-weighted MRI: Reality and challenges, Am. J. Roentgenol. 196 (2011) 1351–1361, http://dx.doi.org/10.2214/AJR.10.5515.
[20] C.A. Clark, D. Le Bihan, Water diffusion compartmentation and anisotropy at high b values in the human brain, Magn. Reson. Med. 44 (2000) 852–859, http://dx.doi.org/10.1002/1522-2594(200012)44:6<852:AID-MRM5>3.0.CO;2-A.
[21] J.H. Jensen, J.a. Helpern, A. Ramani, H. Lu, K. Kaczynski, Diffusional kurtosis imaging: the quantification of non-gaussian water diffusion by means of magnetic resonance imaging, Magn. Reson. Med. 53 (2005) 1432–1440, http://dx.doi.org/10.1002/mrm.20508.
[22] A.B. Rosenkrantz, E.E. Sigmund, A. Winnick, B.E. Niver, B. Spieler, G.R. Morgan, et al., Assessment of hepatocellular carcinoma using apparent diffusion coefficient and diffusion kurtosis indices: preliminary experience in fresh liver explants, Magn. Reson. Imaging 30 (2012) 1534–1540, http://dx.doi.org/10.1016/j.mri.2012.04.020.
[23] G. Pentang, R.S. Lanzman, P. Heusch, A. Müller-Lutz, D. Blondin, G. Antoch, et al., Diffusion kurtosis imaging of the human kidney: a feasibility study, Magn. Reson. Imaging 32 (2014) 413–420, http://dx.doi.org/10.1016/j.mri.2014.01.006.

[24] H.-J. Wittsack, R.S. Lanzman, C. Mathys, H. Janssen, U. Mödder, D. Blondin, Statistical evaluation of diffusion-weighted imaging of the human kidney, Magn. Reson. Med. 64 (2010) 616–622, http://dx.doi.org/10.1002/mrm.2243.
[25] A.B. Rosenkrantz, E.E. Sigmund, G. Johnson, J.S. Babb, T.C. Mussi, J. Melamed, et al., Prostate cancer: feasibility and preliminary experience of a diffusional kurtosis model for detection and assessment of aggressiveness of peripheral zone cancer, Radiology 264 (2012) 126–135, http://dx.doi.org/10.1148/radiol.12112290.
[26] N. Kartalis, L. Loizou, N. Edsborg, R. Segersvård, N. Albiin, Optimising diffusion-weighted MR imaging for demonstrating pancreatic cancer: a comparison of respiratory-triggered, free-breathing and breath-hold techniques, Eur. Radiol. 22 (2012) 2186–2192, http://dx.doi.org/10.1007/s00330-012-2469-3.
[27] A. Rosset, L. Spadola, O. Ratib, OsiriX: An open-source software for navigating in multidimensional DICOM images, J. Digital Imaging 17 (2004) 205–216, http://dx.doi.org/10.1007/s10278-004-1014-6.
[28] G. Weisser, E. Sauter, F. Zöllner, M. Weipert, S. Schoenberg, L. Schad, UMMDiffusion: eine OpenSource software zur klinischen evaluation der kurtosis bildgebung, Fortschr. Rontgenstr. Ger. Congr. Radiol. 186 (S 01) (2014) (p.VO103).
[29] F. Zöllner, S. Kaiser, G. Weisser, L. Schad, UMMDiffusion: an OsiriX plug-in for ADC and IVIM analysis in clinical routine, Salt Lake CIty, USA, in: Proc. Intl. Soc. Mag. Reson. Med., 21, 2013, p. p.3115.
[30] K. Hayano, F. Miura, H. Amano, N. Toyota, K. Wada, K. Kato, et al., Correlation of apparent diffusion coefficient measured by diffusion-weighted MRI and clinicopathologic features in pancreatic cancer patients, J. Hepatobiliary Pancreat. Sci. 20 (2013) 243–248, http://dx.doi.org/10.1007/s00534-011-0491-5.
[31] D. Le Bihan, E. Breton, D. Lallemand, M.L. Aubin, J. Vignaud, M. Laval-Jeantet, Separation of diffusion and perfusion in intravoxel incoherent motion MR imaging, Radiology 168 (1988) 497–505, http://dx.doi.org/10.1148/radiology.168.2.3393671.
[32] D.W. Marquardt, An algorithm for least-Squares estimation of nonlinear parameters, J. Soc. Ind. Appl. Math. 11 (1963) 431–441, http://dx.doi.org/10.1137/0111030.
[33] K. Levenberg, A method for the solution of certain non-linear problems in least squares, Q. Appl. Math. 2 (1944), 196–168 citeulike-article-id:10796881.
[34] H. Lu, J.H. Jensen, A. Ramani, J.A. Helpern, Three-dimensional characterization of non-gaussian water diffusion in humans using diffusion kurtosis imaging, NMR Biomed. 19 (2006) 236–247, http://dx.doi.org/10.1002/nbm.1020.
[35] L. Filli, M. Wurnig, D. Nanz, R. Luechinger, D. Kenkel, A. Boss, Whole-body diffusion kurtosis imaging: initial experience on non-Gaussian diffusion in various organs, Invest. Radiol. 00 (2014) 1–6, http://dx.doi.org/10.1097/RLI.0000000000000082.
[36] A. Lemke, F.B. Laun, M. Klauss, T.J. Re, D. Simon, S. Delorme, et al., Differentiation of pancreas carcinoma from healthy pancreatic tissue using multiple b-values: comparison of apparent diffusion coefficient and intravoxel incoherent motion derived parameters, Invest. Radiol. 44 (2009) 769–775, http://dx.doi.org/10.1097/RLI.0b013e3181b62271.
[37] M. Klauss, A. Lemke, K. Grünberg, D. Simon, T.J. Re, M.N. Wente, et al., Intravoxel incoherent motion MRI for the differentiation between mass forming chronic pancreatitis and pancreatic carcinoma, Invest. Radiol. 46 (2011) 57–63, http://dx.doi.org/10.1097/RLI.0b013e3181fb3bf2.
[38] T.J. Re, A. Lemke, M. Klauss, F.B. Laun, D. Simon, K. Gr??nberg, et al., Enhancing pancreatic adenocarcinoma delineation in diffusion derived intravoxel incoherent motion f-maps through automatic vessel and duct segmentation, Magn. Reson. Med. 66 (2011) 1327–1332, http://dx.doi.org/10.1002/mrm.22931.
[39] K.M. Kang, J.M. Lee, J.H. Yoon, B. Kiefer, J.K. Han, B.I. Choi, Intravoxel incoherent motion diffusion-weighted MR imaging for characterization of focal pancreatic lesions, Radiology 270 (2014) 444–453, http://dx.doi.org/10.1148/radiol.13122712.
[40] K. Sandrasegaran, K. Nutakki, B. Tahir, A. Dhanabal, M. Tann, G.a. Cote, Use of diffusion-weighted MRI to differentiate chronic pancreatitis from pancreatic cancer, AJR Am. J. Roentgenol. 201 (2013) 1002–1008, http://dx.doi.org/10.2214/AJR.12.10170.
[41] M. Takeuchi, K. Matsuzaki, H. Kubo, H. Nishitani, High-b-value diffusion-weighted magnetic resonance imaging of pancreatic cancer and mass-forming chronic pancreatitis: preliminary results, Acta Radiol. 49 (2008) 383–386, http://dx.doi.org/10.1080/02841850801895381.
[42] A.B. Rosenkrantz, B.W. Matza, A. Sabach, C.H. Hajdu, N. Hindman, Pancreatic cancer: lack of association between apparent diffusion coefficient values and adverse pathological features, Clin. Radiol. 68 (2013), http://dx.doi.org/10.1016/j.crad.2012.11.006.
[43] Y. Wang, Z.E. Chen, P. Nikolaidis, R.J. McCarthy, L. Merrick, L.A. Sternick, et al., Diffusion-weighted magnetic resonance imaging of pancreatic adenocarcinomas: association with histopathology and tumor grade, J. Magn. Reson. Imaging 33 (2011) 136–142, http://dx.doi.org/10.1002/jmri.22414.
[44] J.H. Jensen, J.a. Helpern, MRI quantification of non-Gaussian water diffusion by kurtosis analysis, NMR Biomed. 23 (2010) 698–710, http://dx.doi.org/10.1002/nbm.1518.
[45] D.M.J. Lambregts, G.L. Beets, M. Maas, L. Curvo-Semedo, A.G.H. Kessels, T. Thywissen, et al., Tumour ADC measurements in rectal cancer: effect of ROI methods on ADC values and interobserver variability, Eur. Radiol. 21 (2011) 2567–2574, http://dx.doi.org/10.1007/s00330-011-2220-5.